Chapter 5

Diagnosis of a Guided Atom Laser Pulse

This chapter explores the derivation and implementation of a new tomographic technique to ascertain the state of a freely-propagating atomic ensemble; the work in this chapter was presented in the publication:

- *K. L. Moore, S. Gupta, K. W. Murch, and D. M. Stamper-Kurn, Probing the quantum state of a guided atom laser pulse, Phys. Rev. Lett.* ***97****, 180401 (2006). Included in Appendix H.*

Upon observation of the unterminated motion the atom beam launched into the circular waveguide, the following question immediately came to mind: "Is it still a BEC?" For reasons that will be discussed in this chapter, the query itself is ill-posed. Nevertheless, this was the most commonly asked question upon presentation of the ultracold atom storage ring, even to the community of experts working in the field of quantum degenerate atomic systems. The curiosity underlying this problematic question does represent a valid concern, and this chapter will address how to ask and answer the correct formulation of this concern. The answer is of paramount importance if this system is to be viable for atom interferometry, as all contributions to the evolution of the atomic phase under propagation in the circular waveguide must be accounted for.

5.1 Initial Conditions

The central question of this chapter is depicted in Figure 5.1. Succinctly stated, we want to know the quantum state of the atom laser beam as it propagates around the circular waveguide.

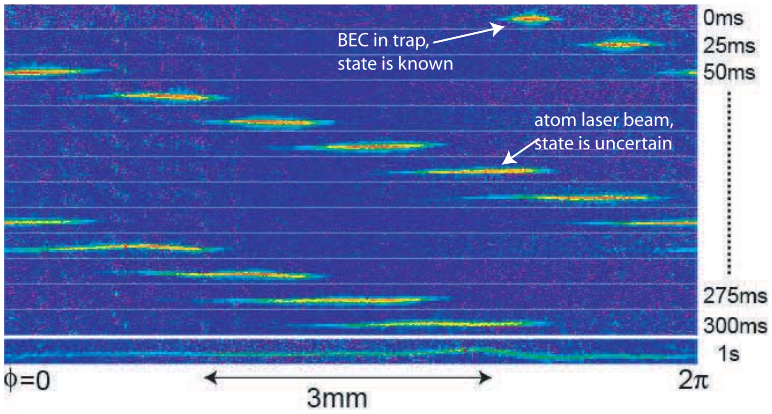

Figure 5.1: Expanding guided atom laser beam

With the general Thomas-Fermi solution for static traps, we input our particular experimental parameters (summarized in Table 5.1) and proclaim with confidence the initial state of the beam. To begin to understand the subsequent state of the system, we first examine the "launch" sequence. This was described briefly in the preceding chapter, but given the known effects of the bias field on the TORT field, we may guess the form of the longitudinal potential $U(\theta)$ experienced by the beam to be

$$U(\theta,t) = \begin{cases} \frac{1}{2}m\omega_\theta^2\left(\rho_o\theta\right)^2 & t < 0 \\ \frac{m\rho_o\Omega\theta}{2}\left(\frac{t}{30\,ms}\right) & 0 \le t < 30\,ms \\ \frac{m\rho_o\Omega\theta}{2}\left(\frac{60\,ms-t}{30\,ms}\right) & 30\,ms < t \le 60\,ms \\ 0 & 60\,ms \le t\,. \end{cases} \tag{5.1}$$

This equation is obtained by a knowledge of the endpoints of the motion, i.e. the initial azimuthal trapping potential ($\frac{1}{2}m\omega_\theta^2(\rho_o^2\theta)^2$) and the final angular velocity (Ω). Any θ dependence beyond the linear terms in the $0 \le t \le 60\,\text{ms}$ would add or subtract to the

m	: Atomic mass of Rb-87	$1.44 \times 10^{-25}\,\mathrm{kg}$
N	: Number of atoms	3×10^5
ρ_o	: Circular trap radius	$1.25\,\mathrm{mm}$
$(\omega_z, \omega_\rho, \omega_\phi)$	: Trapping frequencies (pre-launch)	$2\pi \times (85, 85, 6)\,\mathrm{Hz}$
(ω_T, ω_ϕ)	: Trapping frequencies (post-launch)	$2\pi \times (85, 0)\,\mathrm{Hz}$
a_T	: Transverse oscillator length, $\sqrt{m/2\hbar\omega_T}$	$0.82\,\mu\mathrm{m}$
Ω	: Mean angular velocity of beam.....	*depends on launch*

Table 5.1: Guided atom laser beam parameters.

observed rms momentum width σ_P, which is already fully accounted for by the conversion of the mean-field energy of the cloud into longitudinal kinetic energy. This said, the exact effect of the launching sequence upon the beam is uncertain, and while we can propose models for the evolution from the trapped state into the freely-propagating guided beam state, we must independently verify the state of the beam after the launch and during free propagation.

5.2 Free Evolution in the Circular Waveguide

As the longitudinal potential is "turned off" by balancing the magnetic storage ring, the desired final state is an atomic beam propagating azimuthally while in the ground state of the transverse potential $\frac{1}{2}m\omega_T^2((\rho - \rho_o)^2 + z^2)$. As the mean field energy is converted into kinetic energy on a timescale of $\sim 10\,\mathrm{ms}$ [104], it would seem logical to guess that the transverse state of the beam would evolve to the ground state on the same timescale.

We tested this hypothesis by imaging the beam after variable propagation times in the ring under a relatively slow launch of $\Omega = 2\pi \times 6.3\,\mathrm{Hz}$. The slow launch part is important because, as noted in Table 5.1, the oscillator length is $a_T = 0.82\mu\mathrm{m}$, well below the resolution of our imaging system ($1.8\mu\mathrm{m}$ per pixel at a magnification of 3.7). Thus, time-of-flight imaging must be employed. Of course, for a propagating beam the atoms will not simply drop vertically under gravity, but retain a horizontal velocity of $\rho_o\Omega$. This will carry them to the edges of the 3 mm inner diameter (ID) imaging aperture in a time $\frac{1}{\rho_o\Omega}\sqrt{(ID/2)^2 - \rho_o^2}$ ($= 16.7\,\mathrm{ms}$, in this case). With 15 ms TOF, the rms width of the ground

state oscillator length is 6.6 μm, a size scale our imaging system can resolve. To be sure we are imaging the central width of the beam in the same location (with same magnification, etc.), the rms widths are measured after each period of orbit $T = 2\pi/\Omega = 158$ ms (presented in Figure 5.2).

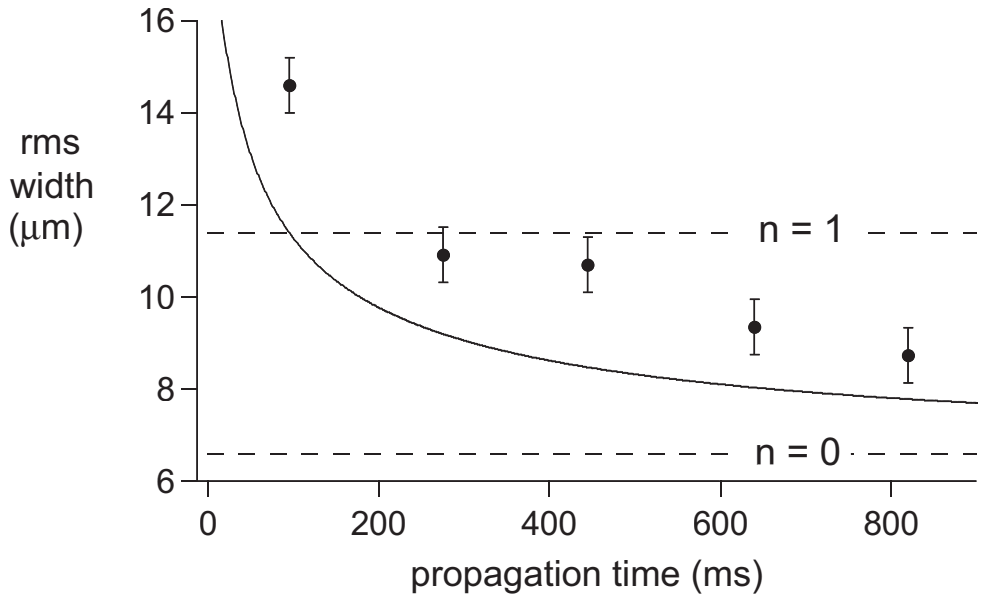

Figure 5.2: Observed transverse widths for atoms pulses after 15 ms TOF. Atoms were launched at very low angular velocity, $\Omega = 2\pi \times 6.3$ Hz. The ground state oscillator length and the first excited state oscillator length (after 15 ms time of flight) are set for reference. The single error bar represents the typical statistical uncertainty in the time-of-flight measurement. Solid line is a 1D model for the transverse width, given experimental parameters.

These data clearly contradict our initial guess of a ~ 10 ms decay to the ground state oscillator length, with the characteristic timescale at least an order of magnitude longer than expected. To account for this discrepancy, we developed a 1-dimensional model for the evolution of the interacting atoms as they freely expanded into the waveguide, roughly following the treatment of Salasnich *et al.* [105]. The prediction of this model is compared to the observed data in Figure 5.2, and while the correspondence between the simplified model and the observed transverse widths is hardly perfect, it is perhaps not terrible for the simplicity of the model. That both the model and the data approach the ground state oscillator length on the same timescale ($\sim$ 100's of ms) indicate that the atomic beam in

the waveguide does appear one-dimensional, with the decay to the transverse ground state oscillator length merely limited by mean-field repulsion. This result gives strong evidence that theoretical considerations of the longitudinal state of the beam, which will occupy the remainder of this chapter, need not consider the transverse state of the beam beyond the predicted values extrapolated from the model. We now focus our efforts solely on the longitudinal state of the beam, a rather involved topic which will consume the rest of this chapter.

5.3 A Note on Coordinates

It will be convenient to treat the system in the rest frame of the propagating atom beam. As the beam is rotating with respect to the lab frame, this may cause some confusion in regards to coordinate systems. To clarify this, we present Figure 5.3 to define the rotating beam coordinates relative to the stationary lab frame. Similarly, Table 5.3 summarizes the coordinate conventions.

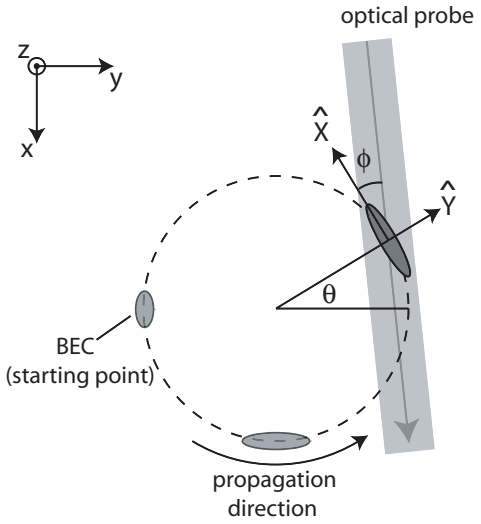

Figure 5.3: Coordinate Axes for the Rotating Atom Beam.

Included is the presence of an optical probe which may illuminate the beam at any position θ in the ring. The relevant coordinate for the optical probe will be the relative

x, y, z : Cartesian coordinates in lab frame, defined (as in chapter 1)
θ : Angular position in ring, measured off y-axis (as in chapter 4)
$\hat{X}$: Propagating axis of the atom beam
X : Longitudinal position, $\rho_o\theta$
σ_X : rms longitudinal width
P : Longitudinal momentum, $\rho_o\Omega$
σ_P : rms momentum width ($= m \times 1.8\,\mu$m/ms)
$\hat{Y}$: Transverse axis of the atom beam
ϕ : Orientation of optical probe relative to the propagating axis of the beam

Table 5.2: Guided atom laser beam coordinate definitions.

angle ϕ between the wavevector of the probe and the longitudinal axis of the beam, $\hat{X}$. These are not to be confused with the stationary axes x, y, z and θ defined in previous chapters.

The remainder of the chapter is concerned with dynamics of the longitudinal coordinate, and the phase space formalism introduced in the next section will be applied to the canonical coordinates X and P, as defined in Table 5.3. As we will show, the system will be characterized entirely by the variables X, σ_X, P, σ_P, and ϕ.

5.4 Phase space Density and the Wigner function

As non-equilibrium systems, particle beams are best understood in the context of a phase space density function $f(\mathbf{r}, \mathbf{p}, t)$ which describes the distribution of particles in phase space with $\int f(\mathbf{r}, \mathbf{p}, t)\, d\mathbf{r}\, d\mathbf{p} = N$, the total number of particles . The evolution of the system is then given by the equation of motion:

$$\left(\frac{\partial}{\partial t} + \frac{\mathbf{p}}{m} \cdot \frac{\partial}{\partial \mathbf{r}} - \frac{\partial U(\mathbf{r}, t)}{\partial \mathbf{r}} \cdot \frac{\partial}{\partial \mathbf{p}}\right) f(\mathbf{r}, \mathbf{p}, t) = \left(\frac{\partial f}{\partial t}\right)_{coll}, \tag{5.2}$$

where $U(\mathbf{r}, t)$ is the potential energy function and $(\partial f/\partial t)_{coll}$ describes the effect of collisions; for dilute gases where binary collisions are dominant, one obtains the Boltzmann transport equation [106]. A wide variety of systems may be understood in this context, spanning an immense energy range from astrophysical phenomena [107] to high-energy beams of charged particles [108] and finally down to the lowest energy scales known to

man, ultracold molecular beams [109, 53]. Full knowledge of the phase space density function and its time evolution completely characterizes a particle beam.

The notion of a phase space density function is predicated upon the assumption that a particle may have a well-defined position and momentum, a supposition which strictly has no validity in the context of quantum mechanics. The phase space picture in quantum mechanics may be recovered through the Wigner quasi-probability distribution [110], and as we have a particle beam which originated from a quantum degenerate source governed by a many-body wavefunction such a treatment would seem appropriate. Proceeding, the single-particle Wigner function is defined relative to a pure quantum state $|\psi\rangle$ as:

$$\mathcal{W}(\mathbf{r},\mathbf{p}) = \frac{1}{2\pi}\int e^{-i\mathbf{p}\cdot\mathbf{a}/\hbar}\psi^*\left(\mathbf{r}-\frac{\mathbf{a}}{2}\right)\psi\left(\mathbf{r}+\frac{\mathbf{a}}{2}\right)d^3\mathbf{a}\,. \tag{5.3}$$

$\mathcal{W}(\mathbf{r},\mathbf{p})$ is the equivalent of the classical phase space density function as $\int \mathcal{W}(\mathbf{r},\mathbf{p})\,d^3\mathbf{p} = |\psi(\mathbf{r})|^2$ and $\int \mathcal{W}(\mathbf{r},\mathbf{p})\,d^3\mathbf{r} = |\widetilde{\psi}(\mathbf{p})|^2$, where $\widetilde{\psi}(\mathbf{p}) = \left(\frac{1}{2\pi\hbar}\right)^{3/2}\int \psi(\mathbf{r})\exp\left(-i\mathbf{p}\cdot\mathbf{r}/\hbar\right)\,d^3\mathbf{r}$ is the momentum-space wavefunction. While the case of a BEC opens the possibility that many particles could occupy the same wavefunction, usually a phase space description is concerned with many particles, perhaps with a statistical mixture of quantum states. All the information about the state of a quantum system is contained in the density matrix $\hat{\rho}$, and the density operator relates to the Wigner function through the equation

$$\mathcal{W}(\mathbf{r},\mathbf{p}) = \frac{1}{2\pi}\int e^{-i\mathbf{p}\cdot\mathbf{a}/\hbar}\left\langle \mathbf{r}-\frac{\mathbf{a}}{2}\right|\hat{\rho}\left|\mathbf{r}+\frac{\mathbf{a}}{2}\right\rangle d\mathbf{a}\,. \tag{5.4}$$

For a free-particle system in the absence of inter-particle interactions the equation of motion for the Wigner function, i.e. the quantum mechanically correct equivalent to the classical Equation (5.2), is given by [111, 112]:

$$\left(\frac{\partial}{\partial t}+\frac{\mathbf{p}}{m}\cdot\frac{\partial}{\partial\mathbf{r}}\right)\mathcal{W}(\mathbf{r},\mathbf{p},t) = \sum_{j=0}^{\infty}\frac{(\hbar/2i)^{2j}}{(2j+1)!}\frac{\partial^{2j+1}U(\mathbf{r},t)}{\partial\mathbf{r}^{2j+1}}\cdot\frac{\partial^{2j+1}\mathcal{W}}{\partial\mathbf{p}^{2j+1}} \tag{5.5}$$

For potentials with no spatial dependence beyond second-order, Equation (5.5) is identical to Equation (5.2), though the Wigner function famously allows $\mathcal{W}(\mathbf{r},\mathbf{p}) < 0$ for certain regions of phase space which may arise from non-classical interference terms. For a system with $U = 0$, the time evolution dictated by Equation (5.5) may be written simply as:

$$\mathcal{W}(\mathbf{r},\mathbf{p},t) = \mathcal{W}\left(\mathbf{r}-\frac{\mathbf{p}t}{m},\mathbf{p},0\right)\,. \tag{5.6}$$

This "shearing" associated with free evolution in phase space introduces an important component of the phase space picture, namely the correlation between position and momentum. Without delving into the details which are more carefully considered elsewhere [113, 114], we can identify the first-order correlation term as $\langle (r_j - \langle r_j \rangle)(p_j - \langle p_j \rangle) \rangle$ on any component of $\mathbf{r}$. If this is non-zero, then the position and momentum of the phase space distribution are not statistically independent (to first order). Under Equation (5.6), this correlation term becomes non-zero for all $t > 0$.

With this architecture in hand we may hypothesize about the evolution of the longitudinal state of the atomic ensemble, with the accuracy of the guess to be checked against the phase space probe developed in the latter part of this chapter. In this vein, three different regimes present themselves. First, there is the condensate regime where the distribution is spread out in X but tightly distributed about $P = 0$. The second regime occurs after the confining potential is extinguished and the mean field energy is converted into kinetic energy. In phase space, this process looks like a vertical shear, driving a strong correlation between position and momentum. The third regime is that of free evolution, as dictated by Equation (5.2). In this regime, the mean field energy is negligible and the beam is freely expanding in the flat waveguide. These three processes are depicted in Figure 5.4.

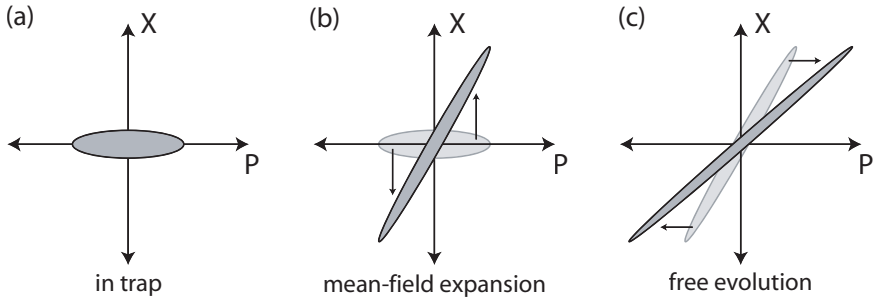

Figure 5.4: Hypothesized phase space evolution. Shown are the three regimes of phase space evolution arising from the launch in Equation (5.1).

With this picture in mind, and our notion of phase space and the Wigner function as the appropriate framework to describe the quantum state of a particle beam, we look for a probe which can ascertain the form of the phase space distribution. The final state can then be described in this context, and since we are considering a system of many particles, the

notion of phase space density remains a useful construction. The distribution of particles will occupy an effective "area" $\mathcal{A}$ in phase space, and this area will be some greater-than-unity multiple of $\hbar$. The ratio of the number of particles to the phase space area of the Wigner distribution yields the phase space density Γ, and under the free evolution both are conserved conserved. As $\Gamma = N$ for a $T = 0$ Bose condensate, we look for a similarly macroscopic phase space density of the propagating beam. We may also borrow a useful notion from particle beams at the other end of the energy spectrum, namely *emittance*. Emittance is employed somewhat in a statement of ignorance of the true phase space area of a beam, but bounds the system by an ellipsoid inside of which the true phase space area must lie [108]. Thus emittance serves as an upper bound on the phase space area, subsequently giving a lower bound on the phase space density.

In this spirit, we posit further that the phase space description of the ultracold atom beam in the circular waveguide can be reasonably described (or at least bounded) by a Gaussian phase space distribution. As the longitudinal width (σ_X) is measurable at all times by absorption imaging and the momentum width (σ_P) is obtained through successive absorption images. An absolute upper bound on the phase space area is obtained by the product $\mathcal{A}_{max} = \sigma_X \sigma_P$. We may be initially comforted by inserting some experimental values into this formula; after just a half revolution in the waveguide the rms longitudinal width was measured to be $\sigma_X = 120\,\mu$m, implying a phase space area of $\mathcal{A} = 310\hbar$. For 3×10^5 atoms, this yields a phase space density of $\Gamma \approx 1000$. This is surely evidence of macroscopic occupation of quantum states, but is a far cry from the presumed initial condition of $\Gamma = N$. Examining Figure 5.4(b) and (c) immediately show that the mere product of the observed σ_X and σ_P could be overestimating the true phase space area in the presence of a strong $X - P$ correlation. Indeed, after both mean field expansion and free evolution we have every reason to believe that there exists a very strong correlation between position and momentum. Taking this into consideration, we may write down a provisional Wigner function for the beam:

$$\mathcal{W}(X,P) = \frac{\exp\left[-\frac{1}{2(1-\eta^2)}\left(\frac{X^2}{\sigma_X^2} - 2\eta\frac{XP}{\sigma_X\sigma_P} + \frac{P^2}{\sigma_P^2}\right)\right]}{2\pi\sigma_X\sigma_P\sqrt{1-\eta^2}}\,, \tag{5.7}$$

where $\eta = \langle XP\rangle/\sigma_X\sigma_P$ is the correlation parameter in the center-of-mass frame of the

beam. The actual phase space area of such a beam is smaller than the aforementioned estimate by a factor $\mathcal{A}/\mathcal{A}_{max} = \sqrt{1-\eta^2}$. Put another way, for proper characterization of a beam with position-momentum correlations one must distinguish between a spatially inhomogeneous momentum width σ_P, which may be dominated by a coherent velocity chirp across the length of the beam, and a "homogeneous" width $\mathcal{A}/\sigma_X$.

While Equation (5.7) is not purported to be an *exact* description of the state, there are numerous reasons to posit this function (not the least of which is its simplicity for the ensuing calculations). Even after many months of launching beams derived from a BEC into motion about the ring, we observed no "smoking gun" which consistently distinguished the distribution as an expanding Thomas-Fermi profile (see Equation (**??**)) versus a Gaussian profile. At the very least, this can again be thought of only as an upper bound on the true phase space distribution, constraining the emittance of the beam.

5.5 Tomographic Imaging of the Wigner Function

In the preceding chapters, *absorption imaging* yielded $x-y$ projections of the three-dimensional spatial density distribution of an atomic population, $n(x,y,z)$, via attenuation of a known light intensity function $I_o(x,y)$ as

$$I(x,y) = I_o(x,y)\exp\left(-\int n(x,y,z)\,\sigma\,dz\right), \tag{5.8}$$

where $I(x,y)$ is the transmitted intensity and σ is the absorption cross section [**?**]. Such imaging is of course impossible for the two-dimensional Wigner distribution $\mathcal{W}(X,P)$, as it is not a function on real space. Spatial images do yield some information about the phase space distribution, however, as the 1D spatial density distribution $n(x)$ is related to the Wigner function of N particles by

$$n(X) = N\int \mathcal{W}(X,P)\,dP. \tag{5.9}$$

This projection has given, at the very least, a spatial bound on the phase space area, but the single line integral of the Wigner function is insufficient to "image" the full two-dimensional distribution $\mathcal{W}(X,P)$.

Tomography is the method by which a two-dimensional function is fully imaged with line integrals such as that in Equation (5.9). The technique relies on a mathematical symmetry between a line integral of a function and a line integral of its fourier transform, formally known as the *Projection-Slice Theorem* [115]. Suppose $f(u,v)$ is an unknown two-dimensional function; its full fourier transform is given by

$$F(k_u,k_v) = \frac{1}{2\pi}\int_{-\infty}^{\infty}\int_{-\infty}^{\infty} f(u,v)e^{-ik_u u}\,e^{-ik_v v}\,du\,dv. \tag{5.10}$$

We now consider a line integral on the y-axis

$$s(u) = \int_{-\infty}^{\infty} f(u,v)dv, \tag{5.11}$$

and its one-dimensional fourier transform

$$S(k_u) = \sqrt{\frac{1}{2\pi}}\int_{-\infty}^{\infty} s(u)e^{-ik_u u}\,du. \tag{5.12}$$

Combining Equations 5.11 and 5.12, we obtain the relation

$$\begin{aligned} S(k_u) &= \sqrt{\frac{1}{2\pi}}\int_{-\infty}^{\infty}\left[\int_{-\infty}^{\infty} f(u,v)dv\right]e^{-ik_u u}\,du \\ &= \int_{-\infty}^{\infty}\int_{-\infty}^{\infty} f(u,v)e^{-ik_u u}\,du\,dv \\ &= \sqrt{2\pi}\,F(k_u,0). \end{aligned} \tag{5.13}$$

The meaning of this relation is that the fourier transform $S(k_u)$ of a projection $s(u)$ of the source function $f(u,v)$ is proportional to a "slice" of the 2D fourier transform $F(k_u,0)$. This procedure can be generalized to any line integral on $f(u,v)$ in a rotated coordinate system ($\tilde{u} = u\cos\vartheta + v\sin\vartheta$, $\tilde{v} = -u\sin\vartheta + v\cos\vartheta$), allowing an infinite set of projections $s(\tilde{u}) = \int_{-\infty}^{\infty} f(u,v)\,d\tilde{v}$ from $0 \le \vartheta < \pi$ to construct the full fourier transform $F(k_u,k_v)$. Applying the inverse transform yields a "reconstruction" of the desired distribution $f(u,v)$, so named because the original function was not directly imaged (as in the case of absorption imaging), but rather inferred from a set of projections $s(\tilde{u})$. A visual representation of this process is shown in Figure 5.5.

The two-dimensional function of interest for a propagating beam is of course the Wigner quasi-probability distribution. We thus seek a probe which yields a signal dependent on the generalized line integral

$$w(\widetilde{X}) = \int_{-\infty}^{\infty} \mathcal{W}(X,P)\,d\widetilde{P}\,. \tag{5.14}$$

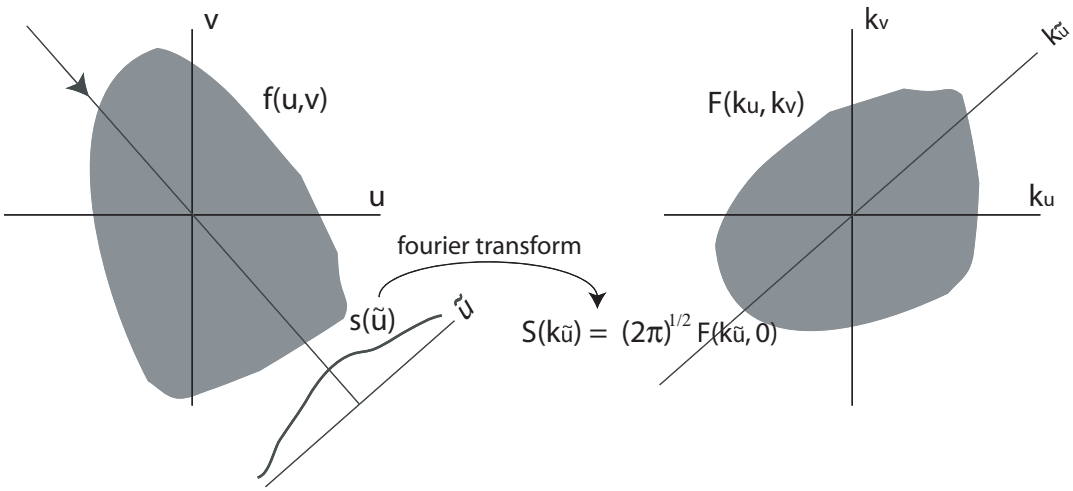

Figure 5.5: The Projection-slice theorem. Fourier transforms of line integrals in coordinate space correspond to slices in fourier space. A set of line integral projections thus clarifies the full fourier transform $F(k_u, k_v)$, and thereby the desired source function $f(u, v)$.

Obtaining the spatial probability distribution $w(X) = \int_{-\infty}^{\infty} \mathcal{W}(X, P)\, dP$ is typically straightforward, but obtaining projections for $\vartheta \neq 0$ is not. Finding and applying a probe capable of resolving a sufficient set of projections $w(\widetilde{X})$ to reconstruct the Wigner function $\mathcal{W}(X, P)$ occupies the remaining sections of this chapter, though we close this section by considering what tomography of the Gaussian Wigner function in Equation (5.7) would look like.

As depicted in Figure 5.6, simple spatial and momentum projections of Gaussian distributions such as that in Equation (5.7) cannot distinguish between correlated and uncorrelated distributions. Because of the functional simplicity of the Wigner function, the off-axis projections can be fully characterized by their rms Gaussian widths. Plotting these widths in Figure 5.6(b) shows that the correlation parameter is revealed in the full set of tomographic projections. The shaded region highlights the limits of allowing free propagation to carry out tomography. It is surely the case that information about σ_X, σ_P, and η can be obtained by absorption imaging after variable times of free propagation. This is tomography, of a sort, with assistance of Equation (5.6), which can be shown to yield

$$\sigma_X^2(t) = \left(\sigma_X^2(0) + \frac{\sigma_P^2}{m^2} t^2\right) + 2\left(\frac{\sigma_P t}{m}\right)\eta\,. \tag{5.15}$$

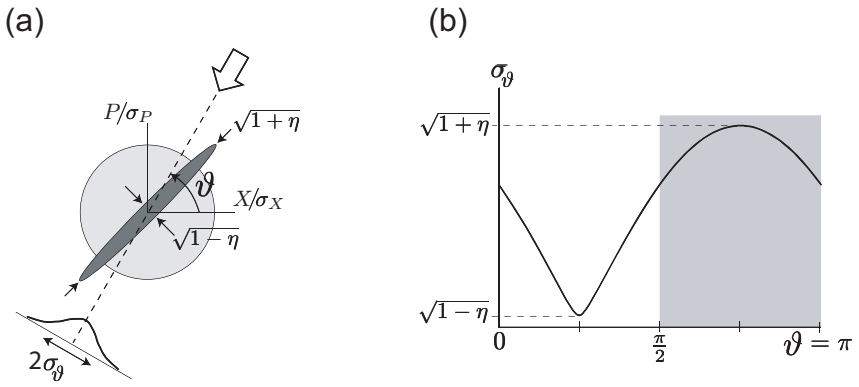

Figure 5.6: Probing a Gaussian Wigner function. (a) Off-axis projections are needed to access the true phase space density. The system is fully characterized by three parameters, σ_X, σ_P, and $\eta = \langle XP \rangle / \sigma_X \sigma_P$. (b) Plot of observed projection widths σ_ϑ show the virtues of tomography, with the widths directly measuring the correlation parameter η. Most desired is the region from $0 < \vartheta < \pi/2$, as the projection along the narrowed axis provides a much more accurate measure of η. The shaded region from $\pi/2 < \vartheta < \pi$ is the region accessible to "time of flight tomography," and fails as an accurate measure of η because for a highly-correlated system $\eta \to 1$.

According to this equation, making a large number of measurements of $|\psi(X,t)|^2$ for $0 < t < \infty$, would allow all three parameters to be extracted. There is a practical problem, however, namely that η is a number very close to unity and is thereby a weak fitting parameter. Ideally one would obtain the set of projections $0 < \vartheta < \pi/2$ as, the minimum value of σ_ϑ at $\vartheta = \pi/4$ gives a normalized width of $\sqrt{1-\eta}$. This is the "most sensitive" angle from which to probe, and is inaccessible to time-of-flight techniques because of the time asymmetry arising from the mean-field expansion, i.e. Equation (5.6) is only valid for $t > 0$. For an arbitrary distribution, projections at all angles $0 \leq \vartheta < \pi$ must of course be obtained to accurately reconstruct the distribution, but for the Gaussian distribution of Equation (5.7) only time-of-flight measurements of σ_X, σ_P, and a single projection along the narrowed axis are required to bound the phase space area.

5.6 Superradiance - A Signature of Coherence

One of the more dramatic signatures of Bose condensation in dilute gases involves the phenomenon known as "superradiance," first elucidated in the seminal work of Robert Dicke in 1954 [116]. Dicke's treatment does not necessitate a Bose-condensed sample, but the topic has seen a substantial revival in interest due to the dramatic superradiant behavior of BECs under certain experimental conditions. The crucial connection between BECs and superradiance is "coherence," and insofar as a BEC represents a macroscopic, many-particle wavefunction with a spatial extent significantly larger than the wavelength of resonant light, the superradiant properties of an ensemble are intimately related with the state of the system.

The details must be omitted here[1], but three factors collude to make superradiant scattering in BECs truly remarkable. The first factor of superradiance is the notion of "end-fire" modes, which come about for a collection of particles which are distributed inhomogeneously in space such that the ensemble is elongated in one direction (say, $\hat{z}$) relative to the remaining two. In this instance, final modes $\mathbf{k}_f = \pm|\mathbf{k}_o|\hat{X}$ which are emitted along the long axis are preferred from the bosonic stimulation (or the effective "bosonic" stimulation in the thermal or even fermionic gases [120]). Bose condensates, especially those confined in the aforementioned optical dipole and Ioffe-Pritchard traps, usually have an elongated axis and thereby strongly scatter along these directions. The second factor which make BECs ideal superradiance testbeds is the "global" coherence of the ensemble atoms, a consequence of the macroscopic occupation of a single quantum state. This will be explored in greater detail in the following section, but simply stated the phase coherence across the spatial extent of the ensemble allows an additive "phased antennae" effect which can cause constructive interference for some output modes and destructive interference for others. The third factor is purely a consequence of the nature of dilute atomic gas BECs, namely that the critical temperatures occur well below the recoil energy $\hbar^2|\mathbf{q}|^2/2m$ associated with the scattering even. This means that the scattered atoms will, under free propagation, separate from the atoms at rest. Counting the number of scattered atoms gives another method, besides the sometimes technically difficult photon detection

[1] We refer the reader to the Refs. [117, 118, 119] for more complete treatments.

of scattered light, to quantify the superradiant scattering rate.

5.7 Superradiance in the Ring

Enacting superradiant light scattering in the ultracold atom storage ring proved to be relatively simple in implementation. We began these experiments with the $\sim 3\times10^5$ atoms in a decompressed $(\omega_T, \omega_\phi) = 2\pi \times (85, 6)\,\mathrm{Hz}$ trap (as compared to the $\omega_\theta = 2\pi \times 35\,\mathrm{Hz}$ trap in the preceding chapter. The atoms were illuminated both in the trap and after the launch, approximately along the $\hat{x}$ direction with laser light $-560\,\mathrm{MHz}$ detuned from the $|^2S_{1/2}, F = 1\rangle \rightarrow |^2P_{3/2}F = 0\rangle$ transition. The light was circularly-polarized, implying that the phase of the TORT field (and therby the orientation of the atomic spins) should be irrelevant for determining the scattering rate[2]. Typical laser intensities were $10\,\mathrm{mW/cm^2}$, yielding single particle Rayleigh scattering rates of $400\,\mathrm{s^{-1}}$, and pulses were of duration $> 50\,\mu\mathrm{s}$ to ensure that we were not in the Kaptiza-Dirac regime (see Section 4.10.2).

After launching the atoms into motion about the ring, we illuminated the atom beam at various incidence angles ϕ and observed the characteristic superradiance effect of elongated Bose condensates, collective scattering out the end-fire mode. As the momentum dispersion of the beam ($\sigma_P = m \times 1.8\,\mathrm{mm/s}$) is nearly an order of magnitude less than the momentum imparted from a superradiant scattering event $2\hbar k = m \times 12.3\,\mathrm{mm/s}$, free propagation in the ring will separate the scattered atoms from the unscattered atoms. This is depicted in Figure 5.7.

Quantifying the superradiant scattering rate has been accomplished previously [117] by direct photocounting of the scattered photons. Despite numerous attempts, we were unable to measure the scattered photons in this system. This is likely due to the small number of scattered photons as well as the "orientation problem," in that at best we would be able to observe the superradiated photons at only a specific angle because the orientation of the superradiating axis is constantly rotating. As shown in Figure 5.7(d), we may quantify the number of superradiant scattering events by counting not photons but recoiling atoms. This most easily done by measuring the longitudinal center of mass,

[2]This was explicitly verified by synchronizing the superradiant light pulse to the TORT fields and varying the phase. As expected, no significant variation of the scattering rate with TORT phase was observed.

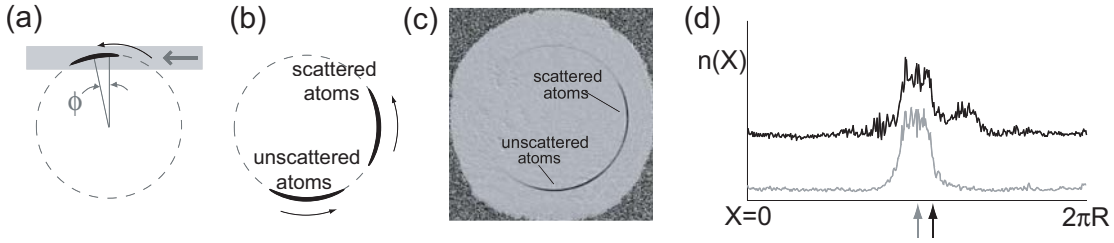

Figure 5.7: Superradiance of the atom pulse propagating in the circular waveguide. (a) Pump light illuminates the freely propagating atom beam at angle ϕ relative to the mean angular position, and (b) scattered atoms separate from the original pulse and can be distinguished from unscattered atoms. (c) Raw image of an atomic beam that has undergone superradiance. The contrast on the image cannot immediately make out Azimuthal density distributions $n(X)$ in the ring 160 ms after illumination are shown for beams that have (black) or have not (grey) undergone superradiant light scattering. The shifted center of mass (indicated by arrows) quantifies the total superradiant scattering rate.

$X_{c.m.}$, given by

$$X_{c.m.} = \frac{\int X\, n(X)\, dX}{\int n(X)\, dX} = \frac{N_{sc}}{N_{tot}} \left(\frac{2\hbar k}{m}\, t \right) , \tag{5.16}$$

where N_{sc} is the number of scattered atoms and N_{tot} is the total number of atoms. N_{sc} is of course a measure of the superradiant scattering rate, but to be useful we must remain in the "small-signal gain" regime [117] where the number of scattered atoms is still small relative to the unscattered atoms. If the superradiant "gain" exceeds the "loss" (which will be discussed extensively in subsequent sections), N_{sc} will increase exponentially and a center-of-mass measurement can be related to the exponential rate.

Using this method, we examined the angular dependence of the outcoupled fraction $f_{sc} = N_{sc}/N_{tot}$ for a given laser pulse of $150\,\mu$s duration and launch of $\Omega = 2\pi \times 9.1\,$Hz, shown in Figure 5.8:

This graph is, strictly speaking, a measurement of gain *minus* loss, so it is not immediately unclear from these data whether the gain, the loss, or both are responsible for the spike in N_{sc} around $\phi = 0$. The contributing factors [117] would not seem to account for the large variation of the overall superradiant gain, so we proceed by attempting to isolate the loss process. As we will see, the mechanism responsible for the angular variation of the superradiant scattering rate in Figure 5.8 is intimately related to the Wigner function of the atomic beam. This fact will be used to provide the desired phase space probe.

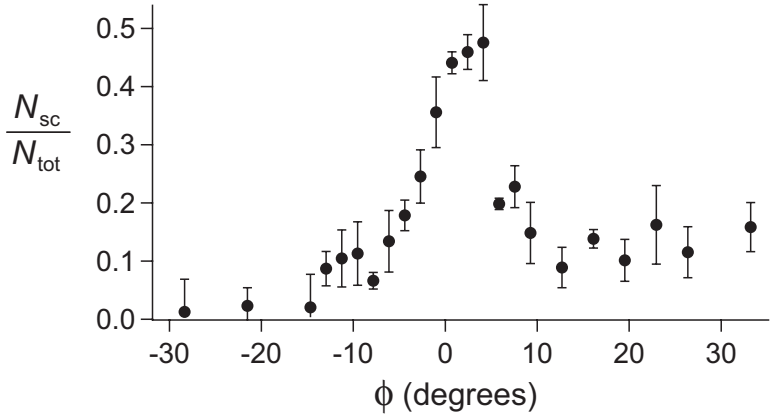

Figure 5.8: Angular dependence of superradiance. The propagating cloud was illuminated at various angles with a single optical pulse of intensity $10\,\mathrm{mW/cm^2}$, detuning $-560\,\mathrm{MHz}$ from the $F = 1 \rightarrow F' = 0$ transition, and duration $150\,\mu\mathrm{s}$. The superradiant population is counted via the center of mass measurements technique in Equation (5.16). These data do not distinguish between the angular dependence of the superradiant gain vs. loss, but do show the dramatic dependence of one or both of these quantities with angle.

5.8 Superradiant Pump-Probe Spectroscopy

Superradiant pump-probe spectroscopy (SPPS) was introduced by Yoshikawa *et al.* [121], and at its core utilizes the "wavefunction overlap" inherent in the superradiant scattering rate to probe the quantum mechanical character of a system. As noted in the preceding section, a BEC is an ideal source for superradiance. Thermal systems would not immediately seem a good source for superradiance given lack of large-scale coherence, but the particles comprising a gas of atoms at temperature T do have a thermal deBroglie wavelength of $\lambda_{dB} = \sqrt{2\pi\hbar^2/mk_BT}$. This sets the "size" of the single-particle wavepackets, as Gaussian wavefunctions with the momentum-space form $\phi(\mathbf{p}) = \exp\left(-\mathbf{p}^2/2mk_BT\right)$.

We humbly rename the technique of Yoshikawa *et al.* as *monochromatic* SPPS, for reasons that will become apparent. In monochromatic SPPS, an initial coherence in a gas is established by initiating superradiant Rayleigh scattering with a laser beam of wavevector $\mathbf{k}_o$ (the "pump" beam). The elongated geometry of the atom beam strongly favors scattering out the endfire mode[3] $\mathbf{k}_f = |\mathbf{k}_o|\hat{X}$, the effect of which is to convert all atomic

[3]This could be either or both $\pm\hat{X}$, with the preference depending on the orientation of the input mode $\mathbf{k}_o$ [122].

wavepackets in the system as $\psi_i(\mathbf{r}) \rightarrow (\alpha + \beta e^{i\mathbf{q}_1\cdot\mathbf{r}})\psi_i(\mathbf{r})$, where $\mathbf{q}_1 = \mathbf{k}_f - \mathbf{k}_o$. The hallmark of superradiance is the exponential growth of $|\beta|^2$ due to corresponding increase in the visibility of the $2\pi/|\mathbf{q}_1|$ density modulation, though this superposition state could be created via other processes, e.g. Bragg scattering.

The system is then allowed to evolve for a time τ, after which the *same* laser beam of wavevector $\mathbf{k}_o$ (now the "probe" beam) illuminates the system and superradiant light scattering is recommenced. That the identical wavevector is utilized for the pump and probe motivates the preface of *monochromatic* SPPS. The scattering rate Γ_{SR} of this pump pulse off the modulated density profile is proportional to square of the phase matching integral

$$\Gamma_{SR} \propto \int d\Omega(\mathbf{k}_f) \left| \int e^{-i(\mathbf{k}_f - \mathbf{k}_o)\cdot\mathbf{r}} \psi^*_{sc}(\mathbf{r},\tau)\psi(\mathbf{r},\tau)\, d^3\mathbf{r} \right|^2 , \tag{5.17}$$

where

$$\psi_{sc}(\mathbf{r},\tau) = \psi\left(\mathbf{r} - \frac{\hbar\mathbf{q}_1}{m}\tau, \tau\right) e^{i\mathbf{q}_1\cdot\mathbf{r}}\, e^{-i\frac{\hbar|\mathbf{q}_1|^2}{2m}\tau} , \tag{5.18}$$

and $\psi(\mathbf{r},\tau)$ is the atomic wavefunction.

End-fire superradiance is still preferred, meaning $\mathbf{k}_f = |\mathbf{k}_o|\hat{X}$ and we find that the superradiant scattering rate is just given by

$$\Gamma_{SR} \propto \left| \int \psi^*\left(\mathbf{r} - \frac{\hbar\mathbf{q}_1}{m}\tau, \tau\right) \psi(\mathbf{r},\tau)\, d^3\mathbf{r} \right|^2 , \tag{5.19}$$

If $\sigma_P \ll \hbar\mathbf{q}_q$, then the argument of Equation 5.19 is just $G^{(1)}\left(\frac{\hbar\mathbf{q}_1}{m}\tau\right)$, the first-order spatial correlation function. The scattering rate thus decreases in time from the increasing *non*-overlap of the initial and scattered atomic wavefunctions. A Gaussian form for the atomic wavefunction will give

$$\Gamma_{SR} \propto \exp\left(-\frac{t^2}{\tau_c^2}\right) , \tag{5.20}$$

where $\tau_c = m/\sqrt{2}|\mathbf{q}_1|\sigma_P$ is the $1/e$ coherence time, and σ_P is the rms momentum width. Yoshikawa *et al.* measured the coherence time for both a thermal gas and partially condensed cloud below T_c, showing a strong divergence in τ_c for the condensate component.

For the purposes herein, we may consider utilizing monochromatic SPPS on the atom beam in the circular waveguide along the elongated propagation axis with a laser beam of wavevector $k_o = \frac{2\pi}{780nm}$. End-fire superradiance will strongly favor backscattering, so

$\mathbf{q}_1 = -2k_o\hat{X}$. The longitudinal momentum dispersion is $\sigma_P = m \times 1.8\,\mathrm{mm/s}$, so the coherence time with the SPPS scheme should be $\tau_c = 24\,\mu\mathrm{s}$.

As we explore in the next sections, carrying out this experiment showed that the coherence time was nearly two orders of magnitude longer than the prediction from monochromatic SPPS! We now introduce *bichromatic* SPPS to explain this dramatic discrepancy.

5.9 Bichromatic Superradiant Pump-Probe Spectroscopy

Motivated by the fact that the guided atom beam is rotating around the circular waveguide, we must reconsider a crucial assumption in the initial consideration of SPPS, namely that the incident laser beam is stationary in time. More generally, the probe pulse may have a different wavevector from the pump laser beam. This may come about from two distinct laser sources of differing color or, more relevantly for the experiments described herein, from a single pump-probe laser source of wavevector $\mathbf{k}_o$ illuminating an atom beam propagating at a rotation rate Ω in the circular atom waveguide. In this case the second probe pulse comes a time τ after the initial pump pulse, the long axis of the atom laser beam will have rotated by an angle $\Omega\tau$. Both possibilities are illustrated in Figure 5.9.

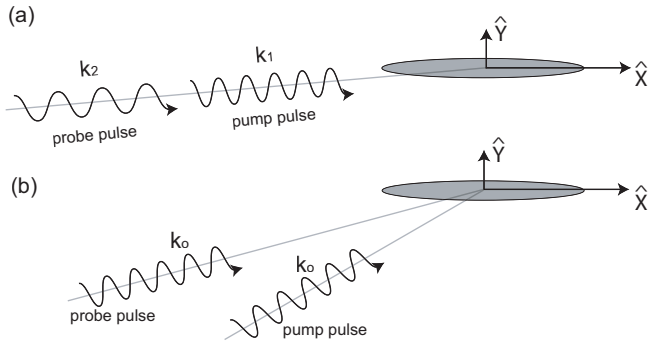

Figure 5.9: Two possible scenarios for bichromatic superradiance pump-probe spectroscopy: (a) The wavevectors of the pump and probe differ, or (b) the incidence angle of the pump and probe differ.

Returning to Equations (5.17) and (5.18), we can retain the necessary generality by

letting $\mathbf{q}_1 = \mathbf{k}_f - \mathbf{k}_1$, the recoil wavevector for the pump pulse, and $\mathbf{q}_2 = \mathbf{k}_f - \mathbf{k}_2$, the recoil wavevector for the probe pulse, differ. As $\hbar\mathbf{q}_1$ exceeds σ_P by a factor of ~ 7, we can also assume the time evolution of the original wavefunction to be negligible on the timescale of τ,[4] meaning $\psi(\mathbf{r}, \tau) \to \psi(\mathbf{r})$. Under the validity of this assumption, the superradiant scattering rate thus becomes

$$\Gamma_{SR} \propto \left| \int e^{i(\mathbf{q}_2 - \mathbf{q}_1)\cdot\mathbf{r}} \psi^* \left(\mathbf{r} - \frac{\hbar\mathbf{q}_1}{m}\tau \right) \psi(\mathbf{r})\, d^3\mathbf{r} \right|^2 , \tag{5.21}$$

Introducing $\mathbf{b} \equiv \hbar\mathbf{q}_1\tau/2m$ and $\Delta\mathbf{q} = \mathbf{q}_2 - \mathbf{q}_1$, we obtain

$$\Gamma_{SR} \propto \left| \int e^{i\Delta\mathbf{q}\cdot(\mathbf{r}-\mathbf{b})}\, \psi^*\left(\mathbf{r} - \mathbf{b}\right) \psi(\mathbf{r} + \mathbf{b})\, d^3\mathbf{r} \right|^2 . \tag{5.22}$$

This equation may be informed further by the inclusion of the momentum-space wavefunction $\widetilde{\psi}(\mathbf{p}) = \left(\frac{1}{2\pi\hbar}\right)^{3/2} \int \psi(\mathbf{r}) \exp\left(-i\mathbf{p}\cdot\mathbf{r}/\hbar\right)\, d^3\mathbf{r}$:

$$\begin{aligned} \Gamma_{SR} \quad \propto \quad & \left| \int e^{i\Delta\mathbf{q}\cdot(\mathbf{r}-\mathbf{b})} \left[\left(\frac{1}{2\pi\hbar} \right)^{3/2} \int \widetilde{\psi}(\mathbf{p}_1) e^{i\mathbf{p}_1\cdot(\mathbf{r}-\mathbf{b})/\hbar} d^3\mathbf{p}_1 \right] \right. \\ & \left. \times \left[\left(\frac{1}{2\pi\hbar} \right)^{3/2} \int \widetilde{\psi}(\mathbf{p}_2) e^{i\mathbf{p}_2\cdot(\mathbf{r}+\mathbf{b})/\hbar} d^3\mathbf{p}_2 \right]\, d^3\mathbf{r} \right|^2 . \end{aligned} \tag{5.23}$$

Further, we define $\mathbf{p} = \left(\mathbf{p}_1 + \mathbf{p}_2\right)/2$ and $\mathbf{p}' = \mathbf{p}_2 - \mathbf{p}_1$. With some algebra, we obtain

$$\Gamma_{SR} \propto \left| \int e^{i\Delta\mathbf{q}\cdot(\mathbf{r}-\mathbf{b})}\, e^{2i\mathbf{p}\cdot\mathbf{b}/\hbar} \left[\int e^{i\mathbf{p}'\cdot\mathbf{r}/\hbar}\, \widetilde{\psi}^* \left(\mathbf{p} - \frac{\mathbf{p}'}{2} \right) \widetilde{\psi} \left(\mathbf{p} + \frac{\mathbf{p}'}{2} \right) d^3\mathbf{p}' \right] d^3\mathbf{p}\, d^3\mathbf{r} \right|^2 . \tag{5.24}$$

The argument inside the brackets is of course the Wigner function $\mathcal{W}(\mathbf{r}, \mathbf{p})$, yielding

$$\Gamma_{SR} \propto \left| \iint e^{i\Delta\mathbf{q}\cdot(\mathbf{r}-\mathbf{b})}\, e^{2i\mathbf{p}\cdot\mathbf{b}/\hbar}\, \mathcal{W}\left(\mathbf{r}, \mathbf{p}\right)\, d^3\mathbf{p}\, d^3\mathbf{r} \right|^2 . \tag{5.25}$$

This equation may appear obscure, but one final change of variables illustrates its meaning. We perform an extended canonical transformation to generalized coordinates, i.e. scaling the position and momentum variables by some r_o and p_o, respectively:

$$\tilde{\mathbf{r}} = \cos\vartheta \frac{\mathbf{r}}{r_o} + \sin\vartheta \frac{\mathbf{p}}{p_o} , \tag{5.26a}$$

$$\tilde{\mathbf{p}} = -\sin\vartheta \frac{\mathbf{r}}{r_o} + \cos\vartheta \frac{\mathbf{p}}{p_o} . \tag{5.26b}$$

[4] A full treatment would merely keep the time dependence $\psi(\mathbf{r}, t)$ and the final results would be largely unaffected (though somewhat obscured).

This substitution takes Equation (5.25) to

$$\Gamma_{SR} \propto \left| \iint e^{i(\Delta\mathbf{q} r_o \cos\vartheta + (2p_o\mathbf{b}/\hbar)\sin\vartheta)\cdot\tilde{\mathbf{r}}}\, e^{i(-\Delta\mathbf{q} r_o \sin\vartheta + (2p_o\mathbf{b}/\hbar)\cos\vartheta)\cdot\tilde{\mathbf{p}}}\, \mathcal{W}(\mathbf{r},\mathbf{p})\; d^3\widetilde{\mathbf{p}}\, d^3\tilde{\mathbf{r}} \right|^2 , \tag{5.27}$$

which has not manifestly improved the situation upon first glance. Recall, however, that $\Delta\mathbf{q} = (\mathbf{q}_2 - \mathbf{q}_1)$ is a parameter under an experimentalist's control in bichromatic SPPS. For instance, it is possible to tune $\mathbf{q}_2$ such that the following condition is satisfied:

$$\Delta\mathbf{q} r_o \cos\vartheta + \frac{2p_o\mathbf{b}}{\hbar}\sin\vartheta = 0\,. \tag{5.28}$$

For this to be valid $\Delta\mathbf{q}$ and $\mathbf{b}$ must be collinear (with respective magnitudes Δq and b). This collinear criterion specifies that $\mathbf{q}_2$, while its magnitude may vary, must be collinear with $\mathbf{q}_1$. This puts a strong restriction on experimental implementations of bichromatic SPPS, indeed such a strong restriction that the implementation in a rotating frame would seem severely hindered. This issue will be revisited, but for now we proceed on the assumption that this criterion can be satisfied.

The phase space angle ϑ is then set by

$$\begin{aligned} \vartheta &= \tan^{-1}\left(\frac{\hbar\Delta q\, r_o}{2p_o b}\right) \\ &= \tan^{-1}\left(\frac{m\Delta q\, r_o}{p_o q_1 \tau}\right) . \end{aligned} \tag{5.29}$$

In this regime, Equation (5.27) becomes

$$\Gamma_{SR} \propto \left| \int e^{i[-\Delta\mathbf{q} r_o \sin\vartheta + (p_o\mathbf{q}_1\tau/m)\cos\vartheta]\cdot\tilde{\mathbf{p}}} \left(\int \mathcal{W}(\mathbf{r},\mathbf{p})\; d^3\tilde{\mathbf{r}} \right) d^3\tilde{\mathbf{p}} \right|^2 . \tag{5.30}$$

Finally, we note that as $\Delta\mathbf{q}$ and $\mathbf{q}_1$ are collinear, we have picked out this axis as "preferred" in that the integrations of $\mathcal{W}(\mathbf{r},\mathbf{p})$ on the two orthogonal axes contribute nothing to the signal. This may be seen through the recognition that the canonical commutation relation $[r_i, p_j] = i\hbar\delta_{ij}$ enforces the separability of the Wigner function in cartesian coordinates

$$\mathcal{W}(\mathbf{r},\mathbf{p}) = \mathcal{W}(r_1,p_1)\,\mathcal{W}(r_2,p_2)\,\mathcal{W}(r_3,p_3)\,, \tag{5.31}$$

with each obeying $\int\int \mathcal{W}(r_i,p_i)\, dr_i dp_i = 1$. Thus, without loss of generality, we may take axis common to $\mathbf{q}_1$ and $\Delta\mathbf{q}$ to define the r_1-axis and integrate out the remaining

dimensions. With this, we obtain

$$\Gamma_{SR} \propto \left| \int e^{i[-\Delta q r_o \sin\vartheta + (p_o q_1 \tau/m)\cos\vartheta]\tilde{p}} \left(\int \mathcal{W}\left(r_1, p_1\right)\, d\tilde{r}_1 \right) d\tilde{p}_1 \right|^2 . \tag{5.32}$$

This equation represents the main result of bichromatic SPPS, and thereby deserves close scrutiny. First, we note that the parenthetical expression represents an off-axis projection of the Wigner function, the necessary element of tomographic phase space imaging, and thus the superradiant scattering signal now depends directly on this function. Second, we note that the remaining integral is the fourier tranform of the off-axis projection. Recalling the projection-slice theorem from Section 5.5, this corresponds to a slice in the fourier transform space of the original function $\mathcal{W}(r_1, p_1)$. Thus, with full experimental control over $\mathbf{q}_1$, $\mathbf{q}_2$, and τ, complete tomography of the six-dimensional $\mathbf{r} - \mathbf{p}$ phase space is accessible.

5.9.1 Bichromatic SPPS with Two Light Sources

The notion of "full experimental control" is obviously the rub. For $\mathbf{q}_2$ to be aligned with $\mathbf{q}_1$ and still achieve tomography, the wavelength of the second light pulse must be different from the first (again, see Figure 5.9). This is experimentally challenging and generally disadvantageous because of the fact that atoms do not Rayleigh scatter all wavelengths equally. (The consequences of differing Rayleigh scattering rates for the pump/probe pulses has not been considered in this analysis.) However, with the use of a second laser a closer examination of Equation (5.29) shows that for a single positive Δq, only $0 \leq \vartheta < \pi/2$ is accessed by mapping scattering rate signals from $0 \leq \tau < \infty$. Swapping the first and second laser pulses has the effect of sending $\Delta q \rightarrow -\Delta q$, completing the complete set of $-\pi/2 < \vartheta < \pi/2$ projection angles necessary for full tomography.

5.9.2 Bichromatic SPPS in a rotating frame

As depicted in Figure 5.9(b), an alternative mechanism to implement phase space tomography is utilizing a single probe laser and probing the Wigner function of a rotating system. This necessitates a revision of Equation (5.32) (though the result will ultimately be retained in the proper limit). In this sub-section we consider the general case of an

atomic beam rotating in a circular 1D waveguide, with the goal being a general result which can then be compared to our experimental parameters in the final section of this chapter.

We begin by considering an elongated beam such as that propagating around a circular waveguide. In the lab frame, the beam is rotating at an angular velocity Ω. We further restrict the system to the two-dimensional plane of the circular waveguide, i.e. the beam motion and pump-probe wavevectors have no z-components. Three length scales must immediately be compared, namely the rms longitudinal width of the beam, σ_X, the rms transverse width of the beam, σ_Y, and the radius of the ring, ρ_o. The following regime is specifically considered:

$$\sigma_Y \ll \sigma_X \ll \rho_o \,. \tag{5.33}$$

The first criterion makes end-fire superradiance with the output mode(s), $\mathbf{k}_f = \pm|\mathbf{k}_i|\hat{X}$, most likely. The second criterion means that the beam subtends a small angular spread $\Delta\phi \approx \sigma_X/\rho_o$, as we will the assign the average angular position to the beam.

As depicted in Figure 5.9(b), the system is illuminated with a pump-probe sequence by a single laser of wavevector k, with pulses separated by time τ. In this separation the probe pulse will have rotated by an angle $\Omega\tau$ with respect to the pump pulse's angle of incidence ϕ, measured off the x-axis. Thus, the following equations are valid:

$$\mathbf{k}_1 = k\left[\cos\phi\hat{X} + \sin\phi\hat{Y}\right] \tag{5.34a}$$

$$\mathbf{k}_2 = k\left[\cos\left(\phi+\Omega\tau\right)\hat{X} + \sin\left(\phi+\Omega\tau\right)\hat{Y}\right) \tag{5.34b}$$

$$\mathbf{k}_f = -k\hat{X} \tag{5.34c}$$

$$\begin{aligned}\mathbf{q}_1 &= \mathbf{k}_1 - \mathbf{k}_f \\ &= k\left[(1+\cos\phi)\hat{X} + \sin\phi\hat{Y}\right]\end{aligned} \tag{5.34d}$$

$$\begin{aligned}\mathbf{q}_2 &= \mathbf{k}_2 - \mathbf{k}_f \\ &\approx k\left[(1+\cos\phi-\Omega\tau\sin\phi)\hat{X} + (\sin\phi+\Omega\tau\cos\phi)\hat{Y}\right]\end{aligned} \tag{5.34e}$$

$$\Delta\mathbf{q} = \mathbf{q}_2 - \mathbf{q}_1 \tag{5.34f}$$

$$\approx k\Omega\tau\left(-\sin\phi\hat{X} + \cos\phi\hat{Y}\right)\,. \tag{5.34g}$$

Where "$\approx$" symbols are used, the assumption that $\Omega\tau \ll 1$ has been made, and as is

typically the case experimentally. These geometric constructions are depicted in Figure 5.10:

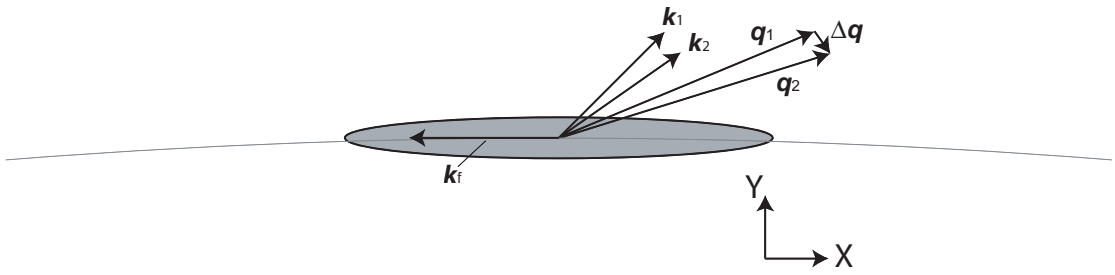

Figure 5.10: Bichromatic SPPS in a circular waveguide.

Returning to Equation (5.25), the generalized phase matching equation, we recast it in two dimensions as:

$$\Gamma_{SR} \propto \left| \iint e^{i\Delta\mathbf{q}\cdot(\mathbf{r}-\frac{\hbar\mathbf{q}_1\tau}{2m})}\, e^{i\mathbf{p}\cdot\mathbf{q}_1\tau/m}\, \mathcal{W}(\mathbf{r},\mathbf{p})\; d^2\mathbf{p}\, d^2\mathbf{r} \right|^2 . \tag{5.35}$$

This may be simplified to

$$\begin{aligned} \Gamma_{SR} \;\propto\; & \left| \iint e^{-ik\Omega\tau\sin\phi X + i\frac{k\tau}{m}(1+\cos\phi)P}\, \mathcal{W}(X,P)\, dX\, dP \right|^2 \\ & \times \left| \iint e^{-ik\Omega\tau\cos\phi Y + i\frac{k\tau}{m}\sin\phi P_Y}\, \mathcal{W}(Y,P_Y)\, dY\, dP_Y \right|^2 . \end{aligned} \tag{5.36}$$

The separability of the two axes is highly advantageous, as we desire a probe solely of the Wigner function of the X-axis and can look at the signal in two pieces, $\Gamma_{SR} \propto \Gamma_{X,SR}\Gamma_{Y,SR}$ as delineated in Equation (5.36). Further, as described in Section 5.2, the transverse state of the beam in a waveguide is dependent upon the longitudinal state of the beam. The rotating system ensures that $\mathbf{\Delta q}$ will *not* be collinear with $\mathbf{q}_1$, so we accept that attempting tomography on one axis will necessarily be "contaminated" by the (quantifiable) effect of the pump-probe sequence on the perpendicular axis or axes.

Proceeding, we look to the $X - P$ integral term in Equation (5.36), and perform the same phase space transformation as conducted in Equation (5.26):

$$\widetilde{X} = \frac{X}{\sigma_X}\cos\vartheta + \frac{P}{\sigma_P}\sin\vartheta\,, \tag{5.37a}$$

$$\widetilde{P} = -\frac{X}{\sigma_X}\sin\vartheta + \frac{P}{\sigma_P}\cos\vartheta\,. \tag{5.37b}$$

Instead of substituting arbitrary spatial and momentum scaling factors, the rms spatial and momentum widths (σ_X and σ_P) are chosen as natural normalization factors. With these, the longitudinal component of Equation (5.36) becomes

$$\begin{aligned}\Gamma_{X,SR} \;=\; &\left|\iint \exp\left[ik\tau\left(-\Omega\sigma_X\sin\phi\cos\vartheta + \frac{\sigma_P}{m}(1+\cos\phi)\sin\vartheta\right)\widetilde{X}\right]\right. \\ &\left.\times\exp\left[ik\tau\left(\Omega\sigma_X\sin\phi\sin\vartheta + \frac{\sigma_P}{m}(1+\cos\phi)\cos\vartheta\right)\widetilde{P}\right]\,\mathcal{W}(X,P)\,d\widetilde{X}d\widetilde{P}\right|^2 .\end{aligned} \tag{5.38}$$

As before, we define ϑ by the satisfaction of the following condition

$$-\Omega\sigma_X\sin\phi\cos\vartheta + \frac{\sigma_P}{m}(1+\cos\phi)\sin\vartheta = 0\,, \tag{5.39}$$

which has the solution

$$\vartheta = \tan^{-1}\left(\frac{m\Omega\sigma_X}{\sigma_P}\frac{\sin\phi}{1+\cos\phi}\right)\,, \tag{5.40}$$

or, equivalently,

$$\vartheta = \tan^{-1}\left(\frac{m\Omega\sigma_X}{\sigma_P}\tan\frac{\phi}{2}\right)\,. \tag{5.41}$$

A crucial difference exists between this rotating case and the preceding example of "linear" bichromatic SPPS, namely that this definition of ϑ has no dependence on τ. This surprising fact is a consequence of the linear-in-time angular variation of $\mathbf{q}_2$, which ultimately cancels with the linear-in-time evolution of the wavefront spacing. Instead of temporal dependence, the phase space angle ϑ is tuned most easily by a variation of ϕ, though Ω is potentially an experimental control knob as well.

Regardless of the method of varying ϑ, the X-component of the superradiant scattering rate is now given by

$$\Gamma_{X,SR} = \left|\int \exp\left[ik\tau\left(\Omega\sigma_X\sin\phi\sin\vartheta + \frac{\sigma_P}{m}(1+\cos\phi)\cos\vartheta\right)\widetilde{P}\right]\left(\int\mathcal{W}(X,P)\,d\widetilde{X}\right)d\widetilde{P}\right|^2 , \tag{5.42}$$

with the desired tomographic projection $\int\mathcal{W}(X,P)\,d\widetilde{X}$ evident in the equation. For completeness, we present the transverse component of the superradiant signal is

$$\Gamma_{Y,SR} = \left|\iint e^{-ik\Omega\tau\cos\phi Y + i\frac{k\tau}{m}\sin\phi P}\,\mathcal{W}(Y,P_Y)\,dY\,dP_Y\right|^2 , \tag{5.43}$$

with the product $\Gamma_{SR} = \Gamma_{X,SR}\Gamma_{Y,SR}$ setting the functional dependence of the superradiant signal. That ϕ sets the $X-P$ phase space angle ϑ yet also contributes to the signal through $\Gamma_{Y,SR}$ means it is incumbent upon the experimentalist to account for the effect of the transverse dimension on the predicted signal. Put another way, Γ_{SR} can only yield tomography on $\mathcal{W}(X,P)$ when the functional behavior of $\Gamma_{Y,SR}$ is fully accounted for, as otherwise the signal is polluted by the transverse contribution.

As a test case, we can imagine enacting bichromatic SPPS on the posited Wigner function in Equation (5.7). Evaluating the line integral with this distribution, we obtain

$$\int \mathcal{W}(X,P)\, d\widetilde{X} = \frac{1}{\sqrt{2\pi\,(1-\eta\sin 2\vartheta)}}\, e^{-\widetilde{P}^2/2(1-\eta\sin 2\vartheta)}\,, \tag{5.44}$$

which is a Gaussian distribution on $\widetilde{P}$ of rms width $\sqrt{1-\eta\sin 2\vartheta}$. Continuing with the evaluation of $\Gamma_{X,SR}$, we have:

$$\begin{aligned}
\Gamma_{X,SR} &= \left| \int \exp\left[ik\tau \left(\Omega\sigma_X \sin\phi \sin\vartheta + \frac{\sigma_P}{m}(1+\cos\phi)\cos\vartheta \right) \widetilde{P} \right] \left(\int \mathcal{W}(X,P)\, d\widetilde{X} \right) d\widetilde{P} \right|^2 \\
&= \left| \int e^{ik\tau\left(\Omega\sigma_X \sin\phi\sin\vartheta + \frac{\sigma_P}{m}(1+\cos\phi)\cos\vartheta\right)\widetilde{P}} \left(\frac{e^{-\widetilde{P}^2/2(1-\eta\sin 2\vartheta)}}{\sqrt{2\pi\,(1-\eta\sin 2\vartheta)}} \right) d\widetilde{P} \right|^2 \\
&= \exp\left[-\frac{m^2k^2}{\sigma_P^2} \left(\frac{1-\eta\sin 2\vartheta}{\cos^2\vartheta} \right) (1+\cos\phi)^2\, \tau^2 \right] .
\end{aligned} \tag{5.45}$$

Recognizing $|\mathbf{q}_1| = k(1+\cos\phi)$ and the parameters in the parenthetical are positive for all ϑ and ϕ, Equation (5.45) becomes simply

$$\Gamma_{X,SR} = \exp\left(-\frac{\tau^2}{\tau_c^2} \right) , \tag{5.46}$$

with τ_c defined as the e^{-1}-decay time,

$$\tau_c = \frac{m}{\sigma_P|\mathbf{q}_1|} \frac{\cos\vartheta}{\sqrt{1-\eta\sin 2\vartheta}} . \tag{5.47}$$

The maximal coherence times will occur at $\vartheta = \pi/4$, the projection along the narrowed axis, yielding

$$\tau_c\big|_{\vartheta=\pi/4} = \frac{m}{\sqrt{2}\sigma_P|\mathbf{q}_1|} \frac{1}{\sqrt{1-\eta}} , \tag{5.48}$$

which corresponds exactly to the monochromatic SPPS signal when $\eta = 0$. Thus, a measurement of the maximal coherence time yields η by

$$\eta = 1 - \left(\frac{m}{\sigma_P|\mathbf{q}_1|\tau_{c,max}} \right)^2 , \tag{5.49}$$

and the bounding phase space area is $\mathcal{A} = \mathcal{A}_{max}\sqrt{1-\eta^2}$. These two equations show that enacting SPPS in the ultracold atom storage ring should (a) result in coherence times much longer than the monochromatic SPPS result would predict and (b) provide the probe we desire to measured the phase space area $\mathcal{A}$.

As previously mentioned, the transverse component $\Gamma_{Y,SR}$ can potentially detract from this measurement of η, so a similar algebraic exercise involving Equation (5.43) can illuminate exactly this contribution to the signal. Under the same Gaussian approximation that correctly predicted the transverse ground state decay, we may envision an *uncorrelated* Gaussian Wigner function with spatial rms width σ_Y. Equation (5.45) then becomes

$$\Gamma_{Y,SR} = e^{-(k^2\Omega^2\sigma_Y^2\cos^2\phi)\,\tau^2} \times e^{-(\hbar^2k^2\sin^2\phi/m^2\sigma_Y^2)\,\tau^2} \tag{5.50}$$

$$= \exp\left(-\frac{\tau^2}{\tau_{c,Y}^2}\right). \tag{5.51}$$

where the transverse decay time $\tau_{c,Y}$ is given by

$$\tau_{c,Y} = \left(k^2\Omega^2\sigma_Y^2\cos^2\phi + \frac{\hbar^2k^2\sin^2\phi}{m^2\sigma_Y^2}\right)^{-1/2}. \tag{5.52}$$

It will depend upon the experimental parameters whether this term will "hide" the long coherence times that Equation (5.47) would afford from the longitudinal term.

5.10 Bichromatic SPPS in the Ultracold Atom Storage Ring

With a theoretical understanding of the issues involved in the bichromatic SPPS signal in a rotating reference frame, we implemented this scheme in the circular waveguide. The angular velocity was $\Omega = 2\pi \times 8.4\,\mathrm{Hz}$, and the earliest time at which the atoms will be approximately aligned with the laser beam occurs after $\approx 61\,\mathrm{ms}$ of propagation time in the ring. At this stage, the atom beam has an rms width of $\sigma_X \approx 120\,\mu\mathrm{m}$, subtending an angle of $\Delta\phi \approx 5.5^o$. This immediately highlights a problematic feature of this incarnation of bichromatic SPPS, namely that the angular spread of the beam potentially compromises the assignment of a single angle ϕ to the system. 2D models which numerically evaluate the azimuthal and transverse phase matching integrals for a curved beam give some credence to the supposition that this is not a problem for this limited extent.

Considering the light pulses themselves, the pump and probe beams were obtained with an SRS pulse generator driving an RF switch (Mini-Circuits ZFSWHZ-1-20) which, in turn, initiated and extinguished the deflection of a beam from an acousto-optic modulator. The pump and probe beams were typically $50\,\mu$s in duration, with the variable delay τ between them. In the duration of the pulses, the atomic beam will rotate by an angle 0.15^o, another effect which detracts from the ideal implementation introduced in the preceding section. In fact, this rotation and the associated rotational dephasing was likely responsible for the angular variations of Γ_{SR} in Figure 5.8, as the beam rotated by an angle 0.49^o during the $150\,\mu$s pulse time.

Experimentally, a systematic measurement of the coherence times at various angles around the ring was even more dramatic than the angular gain picture in Figure 5.8. The sum of the numerous measurements

That the peak is at an angle close, but not equal to zero, makes one suspicious of a systematic error in angular measurement. Unlike superradiance, momentum transfer from Kapitza-Dirac scattering is dependent only on the orientation of the light beams. As the superradiance beam was identical in alignment to the Kapitza-Dirac beam (minus the retroreflection), the axis of scattering seen in Figure 4.14 was the reference for 0^o. The conservative 2^o error estimate is thus based on the uncertainty on the atom beam axis, representing at least 1σ-confidence.

The very long coherence times of $\tau_c \sim 1\,$ms are immediate evidence of a highly correlated system, as they exceed the monochromatic SPPS decoherence time $m/\sigma_P|\mathbf{q}_1| = 35\,\mu$s by a factor of 40. All is not immediately clear, however, as the experimental parameters and an inversion of Equation (5.41) would predict an angle $\phi_c = 31^o$ for these large coherence times to occur, while the data would indicate $\phi_c = 4(2)^o$. This discrepancy is not understood at this time, though we suspect that it may be necessary to adapt our 1D treatment of superradiance to beams with small Fresnel number, i.e., with length greatly exceeding the Rayleigh range defined by the probe wavelength and the transverse width of the atom beam. Our method may be probing only short portions of the beam, the momentum width of which is enhanced by their small extent, rather than probing the beam as a whole.

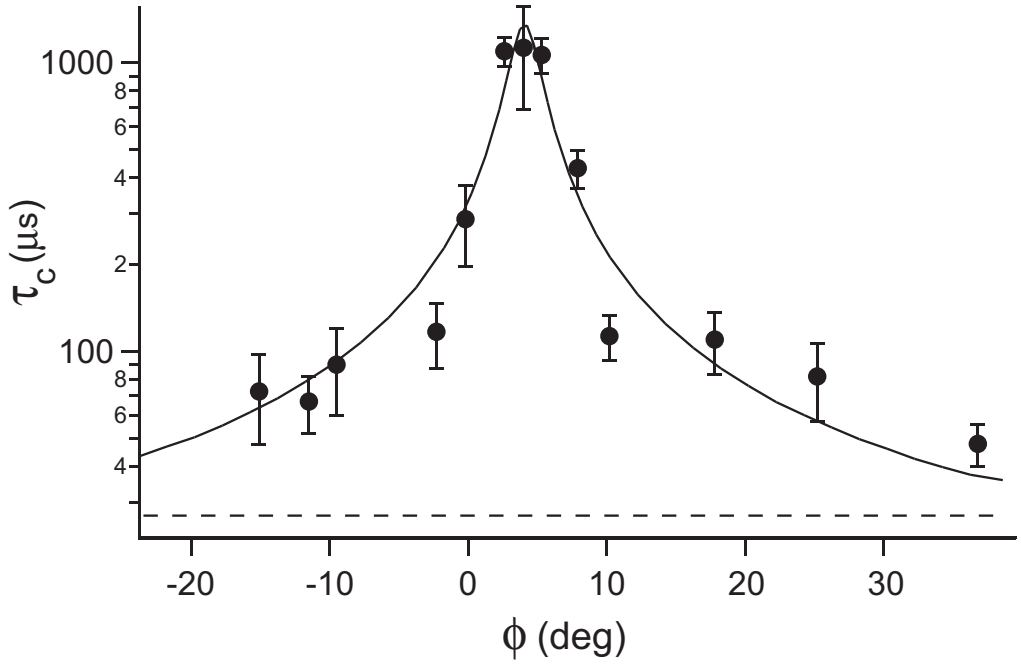

Figure 5.11: Measured coherence times are compared to theoretical predictions for a coherent Gaussian beam (solid line) and an incoherent, uncorrelated ensemble (dotted line). The theoretical curve in fact predicts the maximum coherence time at $\phi = 31^o$ (see text), but has been shifted for comparison to data.

A brief consideration of the transverse contribution to this signal shows that this may be the factor which ultimately limits the observed coherence times. Incorporating experimental values into Equation (5.52) shows the dominant transverse loss to be $\tau_{c,Y} \approx (k\Omega\sigma_Y \cos\phi)^{-1}$. Utilizing the lower bound from the 1D model of Figure 5.2, the transverse width should be $\sigma_Y \approx 2.4\sqrt{\hbar/2m\omega_Y}$. This gives a limiting transverse decay time of $\tau_{c,Y} \approx 1\,\mathrm{ms}$, right in line with the maximum observed coherence time.

Taking the observed maximum coherence time of $\tau_c = 1.1(1)\,\mathrm{ms}$, we infer the correlation parameter to be $\eta = 1 - \left[4.9(6) \times 10^{-4}\right]$. The atom beam is thus constrained to inhabit a phase space area of no more than $\mathcal{A} = 9(1)\hbar$.[5] The constraining Wigner distribution, inside which lies the true distribution, is plotted in Figure 5.12:

This upper bound on the phase space area is presented in lieu of a true reconstructed

[5]This is equivalent to placing a lower bound of $\mathcal{L} = (\hbar|\mathbf{q}|/m)\,\tau_c = 13(1)\,\mu\mathrm{m}$ [123] on the longitudinal coherence length of the propagating cloud.

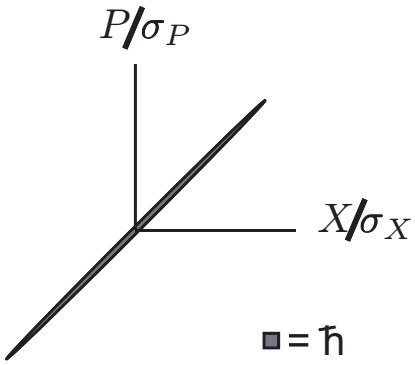

Figure 5.12: Wigner distribution implied by coherence times of 1.1 ms. The phase space area is bounded by $9\hbar$, where an area of $1\hbar$ is shown for reference. In this distribution of ≈ 9 quantum states reside 3×10^5 atoms.

Wigner distribution due to current limitations in data quality (seen in the scatter of Fig. **??**a), though a reconstruction even from the thirteen data points in Fig. **??**b would already yield a distribution of phase space area less than $9\hbar$. This small phase space area further implies a macroscopic phase space density of $N/\mathcal{A} \geq 3.3 \times 10^4$, meaning the beam is still highly degenerate and, if the transverse decay is truly limiting the measurement, possibly fully quantum generate. Thus, our observations should be construed as placing quantitative lower bounds on the coherence of the propagating atom beam while remaining consistent with its complete coherence.

Finally, we note that this effect persisted for multiple orbits about the ring. Figure 5.13 shows the maximal coherence times after 1, 2, and 3 orbits about the ring. All show the same ≈ 1 ms coherence times, implying that the macroscopic phase space occupation is not compromised even after > 300 ms of propagation time. Of particular note is the inset of Figure 5.13(c), which shows that only a small portion of the cloud is undergoing superradiance. This is because at this stage the cloud is subtending a large angular spread of XXX degrees. Because of this expansion, we were unable to make measurements for orbits of greater than three, though we observed nothing which would suggest that the quantum degeneracy is compromised at later propagation times.

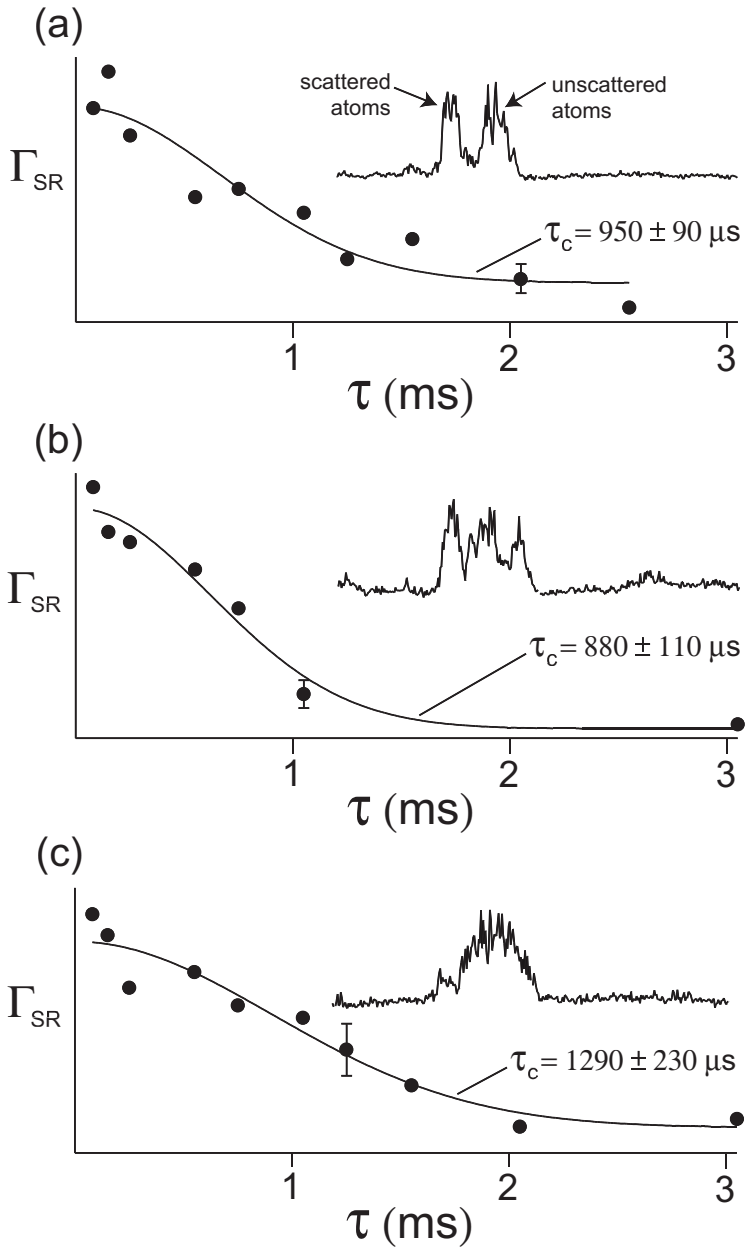

Figure 5.13: Long coherence times after multiple trips around the ring. Insets show typical density profiles $n(X)$ for the respective data series.